OPEN ACCESS



Propagating Alfvénic Waves Observed in the Chromosphere around a Small Sunspot: Tales of 3-minute Waves and 10-minute Waves

Jongchul Chae ¹, Kyuhyoun Cho^{1,2,3}, Eun-Kyung Lim ⁴, and Juhyung Kang ^{1,4}, astronomy Program, Department of Physics and Astronomy, Seoul National University, Seoul 08826, Republic of Korea; jcchae@snu.ac.kr ² Bay Area Environmental Research Institute, NASA Research Park, Moffett Field, CA 94035, USA ³ Lockheed Martin Solar and Astrophysics Laboratory, 3176 Porter Drive, Palo Alto, CA 94304, USA ⁴ Solar and Space Weather Group, Korea Astronomy and Space Science Institute, Daejeon 34055, Republic of Korea Received 2022 March 16; revised 2022 May 7; accepted 2022 May 20; published 2022 July 7

Abstract

Recent observations provided evidence that the solar chromosphere of sunspot regions is pervaded by Alfvénic waves—transverse magnetohydrodynamic (MHD) waves (Alfvén waves or kink waves). In order to systematically investigate the physical characteristics of Alfvénic waves over a wide range of periods, we analyzed the time series of line-of-sight velocity maps constructed from the H α spectral data of a small sunspot region taken by the Fast Imaging Solar Spectrograph of the Goode Solar Telescope at Big Bear. We identified each Alfvénic wave packet by examining the cross-correlation of band-filtered velocity between two points that are located a little apart presumably on the same magnetic field line. As result, we detected a total of 279 wave packets in the superpenumbral region around the sunspot and obtained their statistics of period, velocity amplitude, and propagation speed. An important finding of ours is that the detected Alfvénic waves are clearly separated into two groups: 3-minute period (<7 minutes) waves and 10-minute period (>7 minutes) waves. We propose two tales on the origin of Alfvénic waves in the chromosphere; the 3-minute Alfvénic waves are excited by the upward-propagating slow waves in the chromosphere through the slow-to-Alfvénic mode conversion, and the 10-minute Alfvénic waves represent the chromospheric manifestation of the kink waves driven by convective motions in the photosphere.

Unified Astronomy Thesaurus concepts: Sunspots (1653); Magnetohydrodynamics (1964); Alfven waves (23); Solar atmosphere (1477); Solar chromosphere (1479)

1. Introduction

There is increasing observational evidence that the solar chromosphere of a sunspot hosts magnetohydrodynamic (MHD) waves of different types. It was a long time ago that umbral flashes (Beckers & Tallant 1969), umbral oscillations (Giovanelli 1972), and running penumbral waves (Zirin & Stein 1972) were discovered in sunspot regions, all of which are now understood as the observational manifestation of slow MHD waves, longitudinal and compressive waves that propagate along magnetic field lines.

Magnetized plasma can also host transverse waves that propagate along magnetic field lines. These include Alfvén waves that are fully incompressive and kink waves that are weakly compressive. Even though physically different (Van Doorsselaere et al. 2008), Alfvén waves and kink waves are physically similar to each other and can be mutually converted under a suitable physical condition (e.g., Cranmer & van Ballegooijen 2005). Because of the similarity, it is usually difficult to observationally resolve between these two types. Therefore, both Alfvén waves and kink waves are often referred to as transverse magnetohydrodynamic waves or "Alfvénic waves" without having to distinguish between them.

Detecting Alfvénic waves in the chromosphere of sunspot regions is very important because their presence has been theoretically expected from the consideration of fast-to-Alfvén mode conversion (Cally & Hansen 2011; Khomenko & Cally 2012)

Original content from this work may be used under the terms of the Creative Commons Attribution 4.0 licence. Any further distribution of this work must maintain attribution to the author(s) and the title of the work, journal citation and DOI.

and slow-to-Alfvén mode conversion (Raboonik & Cally 2019; Cally 2022) but has not been well established observationally yet. Detecting Alfvénic waves is challenging because they do not display intensity oscillations, unlike magnetoacoustic waves. They should be detected from the pattern of velocity oscillations instead. Two different methods have been used to detect Alfvénic waves: the imaging method and the spectroscopic method.

The imaging method measures horizontal displacements of well-resolved thread-like features in high-resolution images. This method was employed to detect Alfvénic waves in limb spicules from high-resolution Ca II H images (De Pontieu et al. 2007; He et al. 2009) and those in disk spicules from high-resolution H α images (Jess et al. 2012). The first imaging detection of Alfvénic waves in sunspot regions was done by Pietarila et al. (2011) from the analysis of a superpenumbral fibril seen in Ca II λ 8542 line images. Using the same kind of data and method, Morton et al. (2021) systematically investigated many more events in sunspot fibrils and presented statistics on period, velocity amplitude, and propagation speed.

The spectroscopic method, in contrast, measures line-of-sight (LOS) velocity of fibrils from spectral data. This method can be used even when features are not fully resolved spatially. It was employed by Tomczyk et al. (2007) to detect Alfvénic waves in the corona. The first spectroscopic detection of Alfvénic waves in the chromosphere was done recently by Chae et al. (2021b). They reported LOS velocity oscillations and their propagation that are compatible with Alfvénic waves in the solar chromosphere. Even though Grant et al. (2018) earlier presented the evidence for the Alfvén wave dissipation in the chromosphere of a sunspot using the spectral data of the Ca II $\lambda 8542$ line, they did not provide any evidence for the

detection of Alfvénic waves. The presence of Alfvénic waves was implicitly assumed, and the theoretically calculated temperature enhancement was found to be close to the temperature enhancement inferred from the spectral data. This result can be regarded as indirect evidence for the assumed presence of Alfvénic waves but is irrelevant to direct detection of Alfvénic waves. In contrast, the work of Chae et al. (2021b) was the first clear detection of Alfvénic waves in the chromosphere in that it detected transverse and incompressive velocity oscillations propagating at Alfvén speeds in the direction of magnetic fields.

Note that the spectroscopic method measures the velocity oscillation in the LOS direction, which corresponds to vertical oscillation in near-disk observations, and the imaging method measures the displacement oscillation in the plane of sky, which corresponds to horizontal oscillation in near-disk observations. If the plane of oscillation is obliquely inclined from the LOS direction, the oscillation will be manifest as the LOS velocity oscillation and the plane-of-sky displacement oscillation. If this is the case, the period and propagation speed of the waves should be approximately equal between the two methods. As a matter of fact, we find that the periods and propagation speeds obtained by Chae et al. (2021b) are in good agreement with those found by Pietarila et al. (2011). The Alfvénic waves reported by Morton et al. (2021), however, are apparently different; they have much longer periods and much lower propagation speeds. This contrast suggests that the Alfvénic waves may have a broad distribution of period and the possibility that there might be distinct groups of Alfvénic waves that have different periods and hence different physical origins.

The purpose of the current work is to reveal whether or not there exist different groups of Alfvénic waves in the chromosphere of sunspot regions. For this purpose, we identify as many Alfvénic waves as possible over a wide range of periods from a few minutes to a few tens of minutes by analyzing the LOS velocity data constructed from the spatiotemporal array of $H\alpha$ line spectra. As a result, in fact, we have obtained evidence that there exist two distinct groups of Alfvénic waves: 3-minute period waves and 10-minute period waves.

2. Data and Methods

2.1. Data and Spectral Inversion

We used the ${\rm H}\alpha$ line spectral data taken by the FISS (Chae et al. 2013) of the 1.6 m GST at the Big Bear Solar Observatory (Goode et al. 2010). The specific data used for the current work were taken on 2014 June 3 and are the same as those previously used for the study of shock merging (Chae et al. 2015) and spiral wave patterns (Kang et al. 2019). The FISS repeatedly scanned a small sunspot (pore) region with the spectral sampling of 0.019 Å, the step size of 0.16 (116 km), and the slit-direction sampling of 0.16 (116 km), which covered the field of view of $20'' \times 40''$ (14,500 km \times 29,000 km) every 20 s for 68 minutes.

In order to derive the physical parameters, we applied the technique of multilayer spectral inversion (MLSI; Chae et al. 2020, 2021a) to every spectral profile of the H α line. The MLSI yields the values of 10 free parameters (Chae et al. 2021a), including the LOS chromospheric velocity ν in the top layer, which is the most important parameter in our study, and the four values of the source function: S_p in the photosphere, S_2 around temperature minimum, and S_1 and S_0 in the middle

chromosphere and at the top of the chromosphere. Here S_p corresponds to the photospheric intensity I_p , S_2 corresponds to the temperature minimum intensity $I_{\rm tm}$, and the weighted average of S_1 and S_0 corresponds to the chromospheric intensity I at the $H\alpha$ center. Note that as these intensities are constructed from the source functions, none are affected by Doppler shift, unlike monochromatic images taken at a fixed wavelength of a spectral line. After inversion, we obtained a total of 204 maps for every parameter. All the maps were spatially aligned with the reference image by correcting for image rotation and image displacement. The final form of data to be used for the present study is the 3D arrays of LOS velocity and other parameters. The pixel size is $\delta x = \delta y = 116$ km on the Sun in both directions, and the time step is $\delta t = 20$ s.

2.2. Bandpass Filtering

Here we describe the bandpass filtering of velocity data v, but the same method can be applied to the bandpass filtering of intensity data I as well. In order to detect velocity oscillations of a specific period around P at a point r, we construct the band-filtered time series of velocity $v_b(\mathbf{r}, t; P_l, P_u)$ from the original velocity data $v(\mathbf{r}, t)$. The bandpass filtering is achieved in several steps. First, we construct the trend component $w(\mathbf{r}, t)$ by applying the first-order polynomial fit of t to $v(\mathbf{r}, t)$. Then, we define the lower bound P_l and the upper bound P_u satisfying $P_l \leq P < P_u$, by taking into account the requirement that the period range should be large enough to reveal all the components of the waves but small enough to discard the components of other waves, if any. The chosen value of P_u/P_l usually ranges from 2 to 4. Next, we apply the wavelet decomposition (Torrence & Compo 1998) to $v(\mathbf{r}, t) - w(\mathbf{r}, t)$ and construct the summation of all the wavelets with periods in the range $[P_{I}, P_{II}]$, which after inverse wavelet transforming yields the band-filtered time series $v_b(\mathbf{r}, t; P_l, P_u)$. Note that once the bandpass filtering is applied to all the points in the observing field, we can examine the time series of band-filtered velocity maps. Moreover, it is also possible to construct and examine several sets of band-filtered time series at the same time by choosing multiple sets of P_l and P_u .

Note that the detection of Alfvénic waves of period P from the band-filtered velocity data is most successful when P is significantly longer than P_l and significantly shorter than P_u . If P is close to either P_l or P_u , the detection may not be successful. Thus, for a complete detection of waves of different periods, it is necessary to repeatedly examine different sets of band-filtered velocity data constructed with properly chosen values of P_l and P_u .

2.3. Correlation Analysis

We choose two points r_A and r_B on the same velocity stripe that supposedly trace magnetic field lines, and we examine passband-filtered velocity $v_b(r, t)$. We choose the time range $[t_1, t_2]$ over which the correlations are to be calculated. Then, we calculate the cross-correlation coefficient defined as

$$C(l; \mathbf{r}_{A}, \mathbf{r}_{B}, t_{1}, t_{2}) = \begin{cases} C(a(t_{1}: t_{2} - l\delta t), b(t_{1} + l\delta t: t_{2})) & \text{if } l \geqslant 0\\ C(a(t_{1} - l\delta t: t_{2}), b(t_{1}: t_{2} + l\delta t)) & \text{if } l < 0 \end{cases}$$
(1)

where $a(t_1: t_2 - l\delta ta)$ denotes the array $v_b(\mathbf{r}_A, t_1)$, $v_b(\mathbf{r}_A, t_1 + \delta t)$, \dots , $v_b(\mathbf{r}_A, t_2 - l\delta t)$, and $b(t_1 + l\delta t: t_2)$ denotes the array

 $v_b(\mathbf{r}_B, t_1 + l\delta t), v_b(\mathbf{r}_B, t_1 + l\delta t + \delta t), \dots, v_b(\mathbf{r}_A, t_2)$. The operator C stands for the Pearson cross-correlation coefficient.

Practically, we calculate the value of C(l) for each of $l = -l_M, -l_{M-1}, \dots, -1, 0, 1, \dots, l_M$ with a predefined integer l_M and choose the value of l that maximizes C(l). We found that the correlation is weakened if the time range $(t_2 - t_1)$ is either too short or too long, and the value $(t_2 - t_1)$ in the range from one period to a few periods of velocity oscillations ensures a high value of maximum correlation.

Note that we can determine l with subinteger accuracy by employing the quadratic interpolation of the three correlations around the peak. In order to estimate the accuracy of l, we determined l several times by changing t_1 and t_2 a little bit and estimated their standard deviation. As a result, we find that the accuracy of l is typically estimated at 0.02 for cross-correlation >0.9, but sometimes becomes as large as 0.05. Therefore, we choose 0.05 as a conservative estimate for the standard error of l

If the value of the cross-correlation for l is bigger than 0.90, we decide that we have detected an Alfvénic wave packet. The propagation speed c of this wave packet on the image plane is estimated at

$$c = \frac{|\mathbf{r}_A - \mathbf{r}_B|}{l\delta t}. (2)$$

Here if l is positive, c is positive as well, and it presents the wave packet propagating from \mathbf{r}_A to \mathbf{r}_B . If negative, the wave packet propagates in the reverse direction.

We determine the period of the wave packet based on the autocorrelation analysis. We note that the autocorrelation of a sinusoidal function of period P becomes zero when the time lag $n\delta t$ is taken to be P/4 where n is the value with which the autocorrelation

$$C(n; \mathbf{r}, \mathbf{r}, t_1, t_2) \equiv \mathcal{C}[a(t_1: t_2 - n\delta t), a(t_1 + n\delta t: t_2)]$$
 (3)

becomes zero. The period of oscillation P(r) at a point r is then given by

$$P(\mathbf{r}) = 4n\delta t. \tag{4}$$

Basically, the correlation values are calculated for integer values of n using the above expression. Then, by applying the linear interpolation of two correlation values that are closest to zero, we determine n with subinteger accuracy. The period of the wave packet $P(\mathbf{r}_A, \mathbf{r}_B)$ propagating from \mathbf{r}_A to \mathbf{r}_B is then determined from the two values $P(\mathbf{r}_A)$ and $P(\mathbf{r}_B)$ by taking their geometric average

$$P(\mathbf{r}_A, \mathbf{r}_B) \equiv \sqrt{P(\mathbf{r}_A)P(\mathbf{r}_B)}.$$
 (5)

In fact, it is expected that $P(\mathbf{r}_A) = P(\mathbf{r}_B) = P(\mathbf{r}_A, \mathbf{r}_B)$ when the cross-correlation of velocity between the two points is very close to 1

Now we determine the velocity amplitude of oscillation V at point A using the expression

$$V(\mathbf{r}; t_1, t_2) \equiv \sqrt{2} S[a(t_1 : t_2)],$$
 (6)

where the operator S refers to the standard deviation. Using this expression, we can define the velocity amplitude of the

wave packet $V(\mathbf{r}_A, \mathbf{r}_B)$ propagating from \mathbf{r}_A to \mathbf{r}_B as

$$V(\mathbf{r}_A, \mathbf{r}_B) \equiv \sqrt{V(\mathbf{r}_A)V(\mathbf{r}_B)}. \tag{7}$$

3. Results

3.1. Magnetic Environment

Figure 1 provides some information on the magnetic environment of the observed region. The photospheric intensity indicates that the sunspot is a regular pore, being small and roundish, and not having a penumbra. The temperature minimum intensity displays numerous bright points and faint network structures. These fine-scale features are useful for the spatial alignment of the FISS images and the magnetogram data taken by the SDO/HMI, with the accuracy of better than, say, 0."2. The map of chromospheric intensity displays a number of dark threads (fibrils) and bright threads outside the sunspot where the LOS fields in the photosphere are weak. The fibrils here correspond to superpenumbral fibrils seen outside the penumbra of a large sunspot. The contour of 250 G level roughly marks the boundary between stronger field regions inside the sunspot and fibril regions outside it.

It appears that the long and stable fibrils in the lower half of the field of view are supported in the chromosphere by predominantly horizontal magnetic fields. We have constructed the magnetic fields in the chromosphere by employing the potential field extrapolation of the HMI magnetogram of $512'' \times 512''$ area. The figure clearly shows that dark threads (fibrils) and bright threads are well aligned with the field lines constructed from the potential field extrapolation, despite the reported concern that some fibrils might not be aligned with local magnetic fields (de la Cruz Rodríguez & Socas-Navarro 2011). We also find that velocity stripes radially extended out of the sunspot are also aligned with the field lines, even though these structures are often a little broader and less clearly discernible than the intensity threads. Therefore, we conclude that both intensity threads and velocity stripes are fairly well aligned with predominantly horizontal magnetic field lines.

The predominantly horizontal nature of magnetic fields in the fibril regions is clearly demonstrated by the plots of the sample field line shown in Figure 2. The LOS field of this field line was 433 G at its footpoint. The figure shows that the elevations of the field line are small below 3000 km at distances up to 10,000 km, and the inclination from the vertical is high, being around 80° at most parts, confirming the predominantly horizontal nature of magnetic fields in the chromosphere. The figure also shows that magnetic field strength ranges from 300 G at distance 2000 km to 70 G at distance 8000 km. We have examined the dependence of the constructed field line on the footpoint. If a point closer to the center of the sunspot is selected as the footpoint, the constructed field line has higher altitudes and lower inclinations, as expected. Despite these subtle variations, we confirm that all the field lines constructed from the points around the edge of the sunspot (defined by the LOS field of 250 G) are predominantly horizontal. Moreover, we found that the field strengths along these field lines are almost independent of height and are given as a function of horizontal distance only. Therefore, we can use this variation shown in Figure 2 for

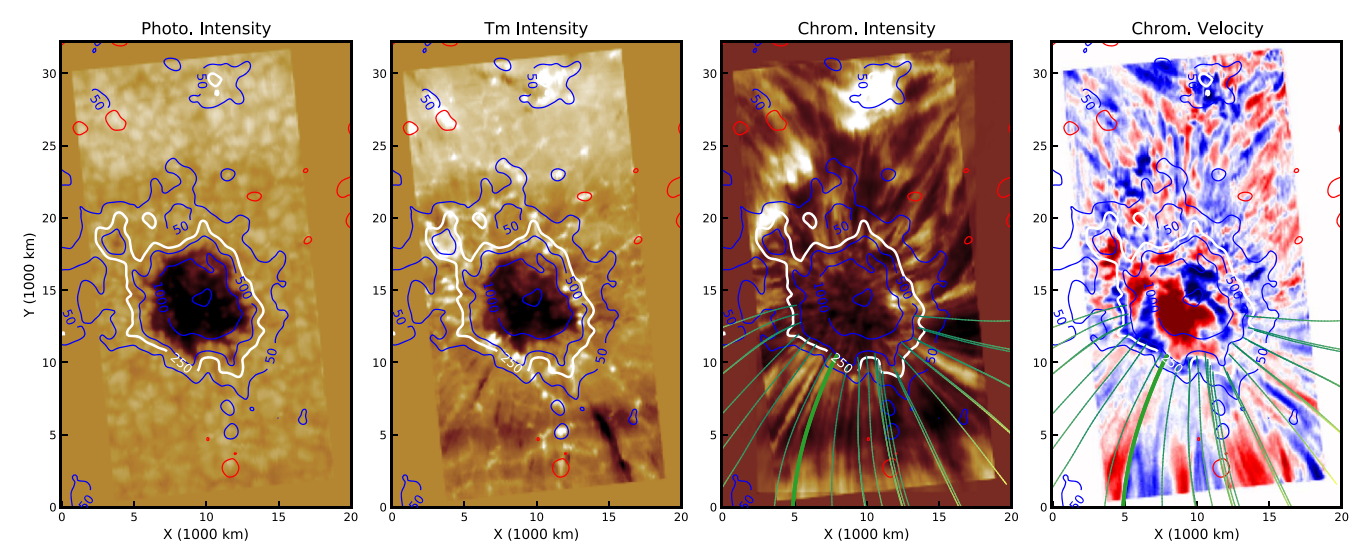


Figure 1. Maps of photospheric intensity $I_{\rm ph}$, temperature minimum intensity $I_{\rm tm}$, chromospheric intensity I, and band-filtered (1.5–3.0 minutes) chromospheric velocity v_b taken at 17:00:00 UT of 2014 June 3. Superposed on the images are the contours of LOS magnetogram taken by the SDO/HMI at the same instant as above. The contour levels are -50 (red), +50 (blue), 250 (white), 500, 1000 and 1500 G (blue). The radially directed curves plotted over the maps of I and v_b are the image-plane projection of some potential magnetic field lines constructed with the footpoints being put at regions of LOS magnetic field 250–500 G. The thick curve is the sample field line examined in detail in Figure 2.

illustration as a good proxy of the general variation of field strength over horizontal distance from the edge of the sunspot.

3.2. Slow Magnetoacoustic Waves and Alfvénic Waves in the Sunspot Region

Slow magnetoacoustic waves and Alfvénic waves are similar to each other in that they propagate along magnetic fields. Both the types can be identified from our observations. Slow waves are well detected inside the sunspot where magnetic fields are predominantly vertical in the chromosphere. Alfvénic waves can be well detected in the superpenumbral region around the sunspot where magnetic fields are predominantly horizontal in the chromosphere.

The oscillations of velocity seen inside the sunspot (see Figure 3) are longitudinal oscillations along magnetic fields and hence represent slow magnetoacoustic waves propagating in a gravitationally stratified medium. The top panel of Figure 4 indicates that the time variation of velocity at a point inside the sunspot is well correlated with that of intensity, especially in the band-filtered (1.5–3.0 minutes) data, which supports the compressive nature of the oscillations. Note that the phase difference between intensity and velocity is close to $\pi/4$, which is the property of dispersive slow magnetoacoustic waves with periods close to the acoustic cutoff (e.g., Chae & Litvinenko 2017).

The time series of velocity maps reveal the spatiotemporal pattern that the concentric or spiral pattern of longitudinal oscillation propagates radially out of a point inside the sunspot, as previously reported by Kang et al. (2019). The speed of propagation is higher than the sound speed, being in line with the previous reports on horizontal wave propagation observed in the lower atmosphere inside sunspots (Zhao et al. 2015; Cho et al. 2019). This horizontal propagation, however, is not real but apparent. The apparent propagation can be understood as a consequence of the successive excitation of the slow waves in the photosphere by the fast waves that originate from the same subsurface source and successively arrive at different regions in the photosphere (Cho & Chae 2020).

On the other hand, the oscillations of LOS velocity in the superpenumbral region outside the sunspot are transverse oscillations across magnetic fields (see Figure 3) because magnetic fields here are predominantly horizontal as described above. The absence of the cross-correlation between velocity and intensity shown in the bottom panel of Figure 4 confirms that these oscillations are incompressive. Note that the intensity fluctuates with time, but these fluctuations are not strongly correlated with velocity and hence may not be attributable to the compressive waves. We have examined the correlation at many other points and reached the conclusion that in general the correlation is the strongest inside the sunspot, is fairly strong near its boundary, and is practically absent in the superpenumbral region much outside its boundary.

We also find that the spatial pattern of velocity outside the sunspot is different from the pattern inside the sunspot. We see a number of velocity stripes radially extended out of the sunspot, which are very well aligned with either dark intensity threads (fibrils) or bright threads. Velocity stripes, however, are not necessarily confined to individual intensity threads. A velocity stripe is often broader than an intensity thread and spans more than one thread, either dark or bright. This may be because velocity oscillations in the adjacent field lines are excited by the same source and propagate along the field lines with about the same phase. The occurrence of the velocity stripes radially extended implies the presence of waves propagating at fast speeds along magnetic field lines. These are the Alfvénic waves we investigate.

We emphasize that the detection of velocity oscillations using the spectroscopic method does not require the clear identification of intensity threads. Intensity may change with time, but velocity measurement can be done irrespective of this change. In addition, the spectroscopic method is free from the concern that the same fibril may sample different field lines at different times (Leenaarts et al. 2015), which arises when oscillations are to be measured from the displacement of fibrils.

The time-distance plots of intensity and velocity shown in Figure 5 indicate the presence of Alfvénic waves outside the sunspot. We first consider the region close to the footpoint

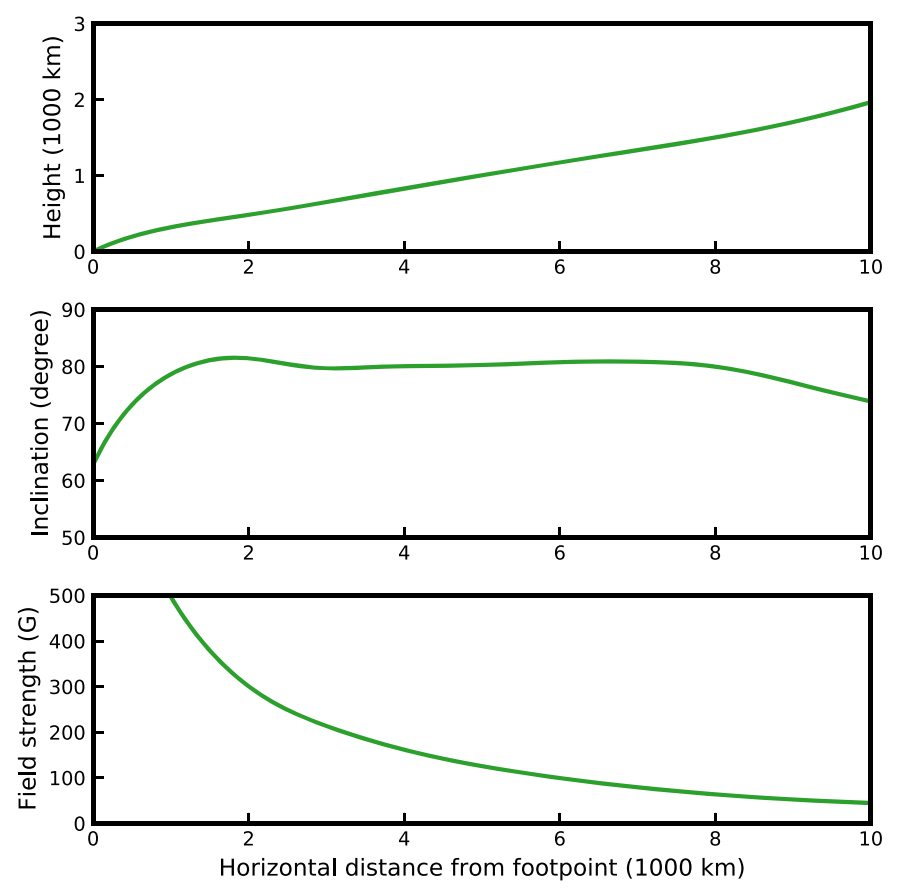


Figure 2. Plots of height (top), inclination (middle), and magnetic field strength (bottom) of the sample field line (represented by the thick green curve in Figure 1) vs. the horizontal distance from its footpoint.

(<1000 km). Here velocity oscillations are strongly correlated intensity oscillations, and the propagation speed inferred from the slope is typically 10 km s⁻¹. These are slow magnetoacoustic waves. As they occur near the edge of the sunspot (pore), they may be considered as the pore version of running penumbral waves. The observed propagation may be the projected view of slow waves propagating along inclined magnetic fields like in running penumbral waves (Bloomfield et al. 2007). In contrast, at regions much away from the footpoint (>1000 km), velocity oscillations are not correlated with intensity oscillations at all, supporting the absence of intensity-velocity correlation in these regions far from the sunspot. Mover, the speed of propagation as inferred from the slope of a velocity stripe is very high, typically 100 km s⁻¹. Together with the transverse nature of the velocity oscillations, these two properties are very compatible with Alfvénic waves.

3.3. Identification and Measurement of Alfvénic Waves

The detection of Alfvénic waves and the parameter determination require a careful analysis of the data because Alfvénic waves occur with very high speeds and within a limited range of space and time in the form of packets rather than trains. We found that the technique of cross-correlation of band-filtered velocity oscillations at two points is quite useful for the required analysis. The detection of each Alfvénic wave packet consists of a few steps. First, by inspecting the maps of intensity and velocity at a specific time by eye, we identify a velocity stripe, as well as the suitable passband (period range).

Next, we select two points that are on this velocity stripe and are well aligned with the intensity threads that are supposed to follow local magnetic field lines. Then, we inspect the time variations of velocity at these two points and choose a time interval as long as possible for the correlation analysis. If the velocity variations at the two points are strongly correlated $C_m(l) > 0.9$, have significant velocity amplitudes $V(\mathbf{r}_A) > 0.25$ km s⁻¹ and $V(\mathbf{r}_B) > 0.25$ km s⁻¹, and have a sizable time lag l > 0.15, then we identify them as an Alfvénic wave packet. Sometimes the time lag between two points is very close to zero. This case may be interpreted as either propagating waves of very high propagation speed or standing waves and so on. Here we limit our study to propagating waves with finite propagation speeds by requiring the time lag to be finite enough.

Figure 3 show two points selected at a time for illustration: X (marked by a cross) and Y (marked by a plus sign). They are located on a velocity stripe clear in the map of the band-filtered (3–7 minutes) velocity. The distance between these points is 1350 km. Figure 6 shows that the velocity oscillations at the two points are correlated with each other with time lag. We choose the time interval as indicated in the figure. The cross-correlation is found to be the strongest in the passband (3–7 minutes). The cross-correlation is as high as 0.96, and the detected time lag is 0.85 step, or about 17 s. This time lag, combined with the above distance, yields about 80 km s⁻¹ as the estimate of the propagation speed of the wave packet on the image plane. The positive value means that the wave packet propagates from X to Y, namely, outward from the sunspot. The

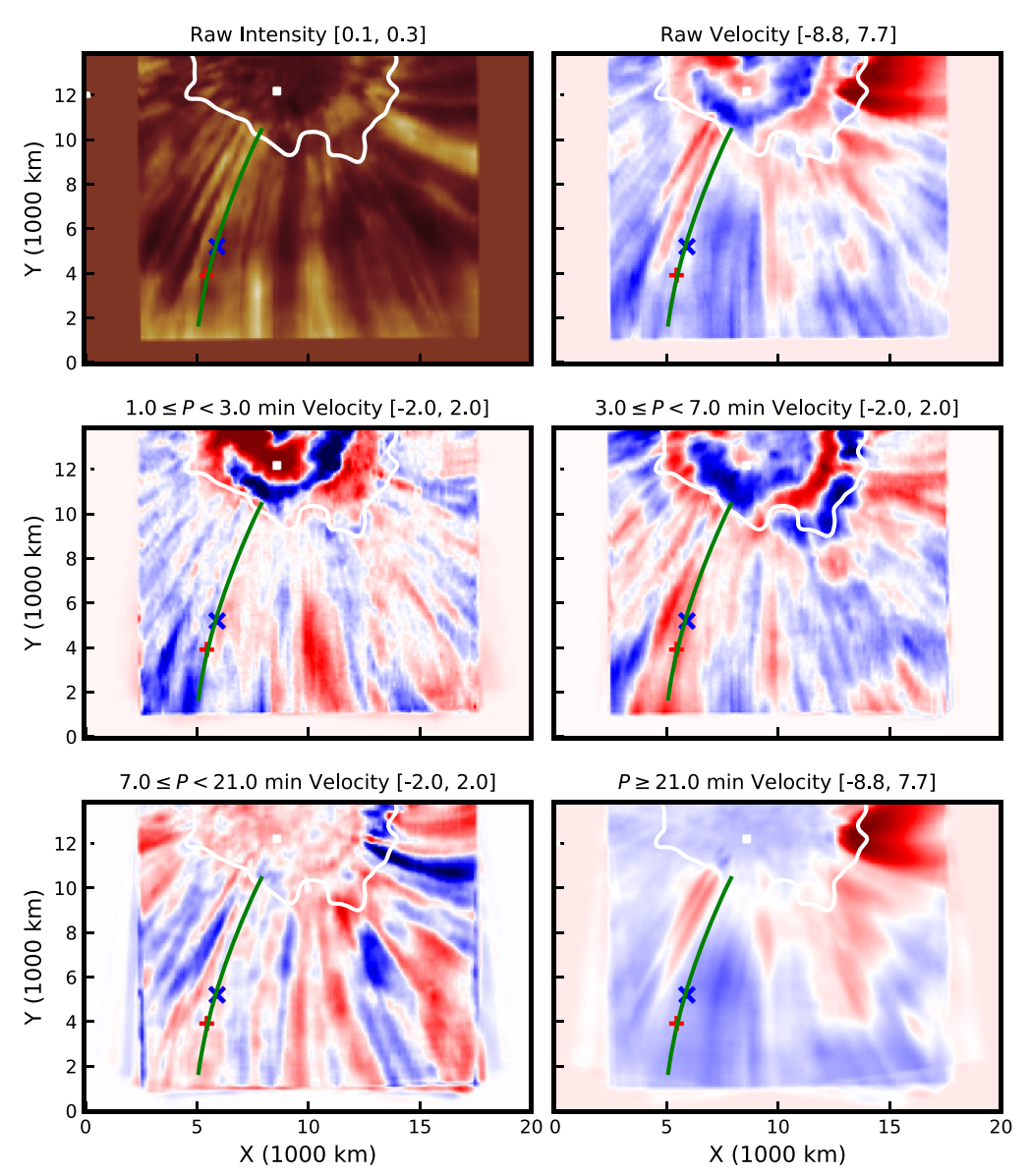


Figure 3. Maps of $H\alpha$ intensity constructed from the source function parameters (top left), original LOS velocity (top right), band-filtered velocities (middle panels and bottom left), and long-period-filtered velocity (bottom right). The intensity is measured in units of continuum intensity averaged over the observed region, and velocity is measured in units of km s⁻¹. The lower and upper bounds of each passband are indicated in each panel. The numeric values in the brackets of each map are the lower and upper bounds for byte-scale display. The red color corresponds to the upper bounds of LOS velocity (redshift), and the blue color corresponds to the lower bounds (blueshift). The oscillations at the points marked by the white square and the cross, respectively, are presented in Figure 4. The green curve is a part of the sample field line indicated in Figure 1 and also represents the cut slit along which were constructed the time—distance plots of intensity and velocity as shown in Figure 5. The oscillations at the two points marked by a cross (X) and a plus sign (Y) are presented together in Figure 6.

period of the wave packet is estimated at 4.5 minutes, and its velocity amplitude is estimated at 0.47 km s^{-1} .

3.4. Statistics of the Parameters

We have identified a total of 279 wave packets. Figure 7 presents the number distributions of their period P, propagation speed c, and velocity amplitude A. Note that we examine the statistics of these parameters using their logarithmic values; the binning for the histogram is done to the logarithmic values, and the mean values and standard deviations are taken over the logarithmic values as well, which are summarized in Table 1.

We find from the top of Figure 7 that P is distributed over a wide range of period. The distribution, however, is not singly peaked. It consists of two components: a component peaked around 3 minutes (3-minute period waves), and another

component peaked around 10 minutes (10-minute period waves). The separation between the two components occurs around P=7 minutes. A total of 145 identified wave packets are categorized into the 3-minute waves, and a total of 134 wave packets are categorized into the 10-minute waves. The mean and standard deviation of $\log P$ for waves of P<7 minutes are 0.57 and 0.14, from which we can say that the period P of 3-minute waves is $10^{0.57}=3.7$ minutes on average and ranges from $10^{0.57-2\times0.14}=1.9$ minutes to $10^{0.57+2\times0.14}=7.1$ minutes. In the same manner, it is found that the period P of 10-minute waves is 12 minutes on average and ranges from 6.6 to 22 minutes. The period range of the 3-minute waves includes all the periods from 2.5 to 4.5 minutes reported by Chae et al. (2021b) based on the spectroscopic detection and the period of 2.3 minutes reported

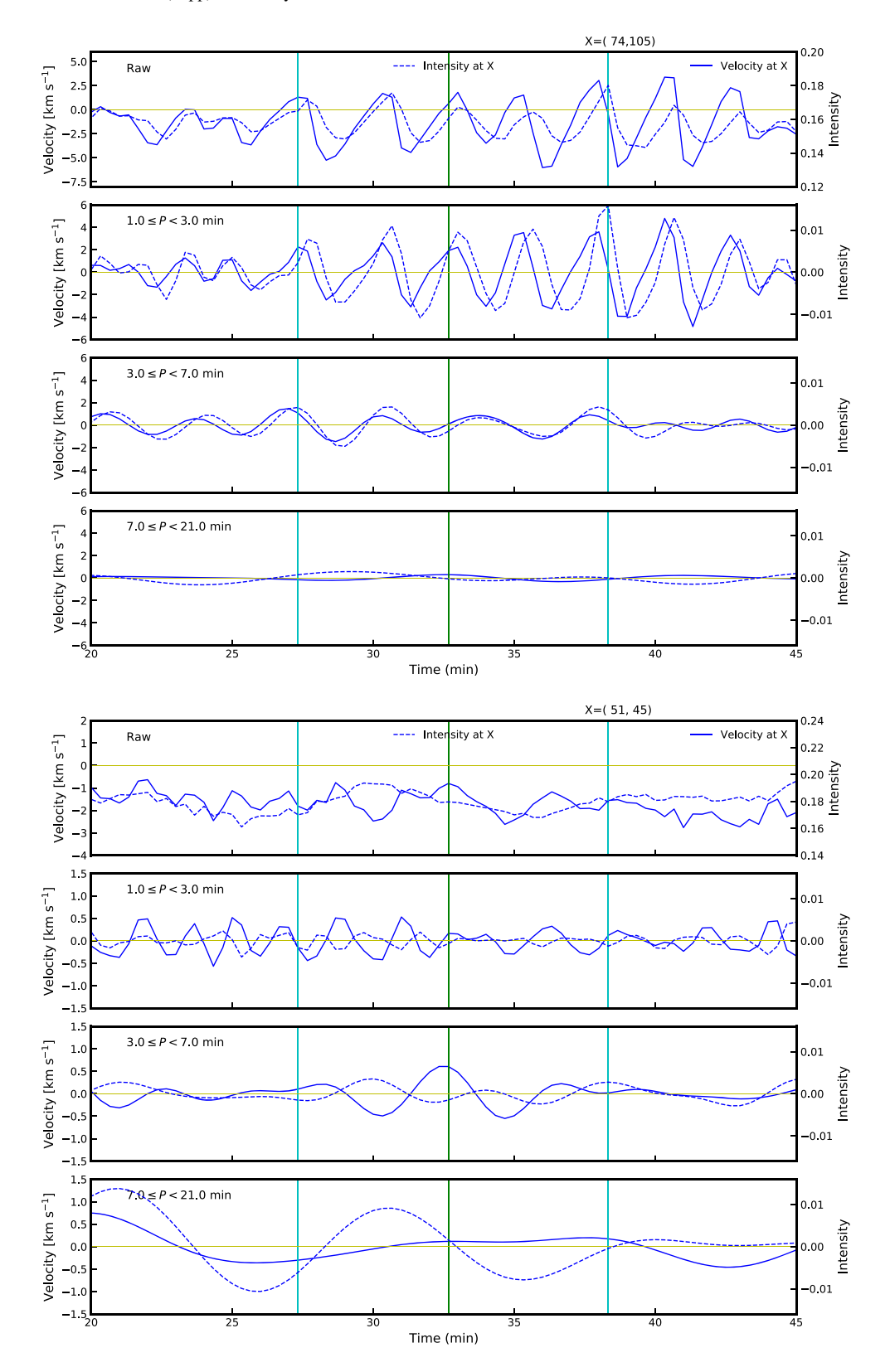


Figure 4. Plots of velocities and intensities vs. time at the point (marked by a square in Figure 3) inside the sunspot (top) and at a point (marked by a cross) in the superpenumbral region outside the sunspot.

by Pietarila et al. (2011) based on the imaging detection. The period range of the 10-minute waves is compatible with the distribution of periods with the mean of 12.6 minutes reported by Morton et al. (2021) based on the imaging detection.

We examine the statistics of propagation speed c in the same way as above. The middle panel of the figure shows the number distribution of propagation speed c. The mean and the standard deviation of $\log c$ for the 3-minute waves are 2.15 and 0.32,

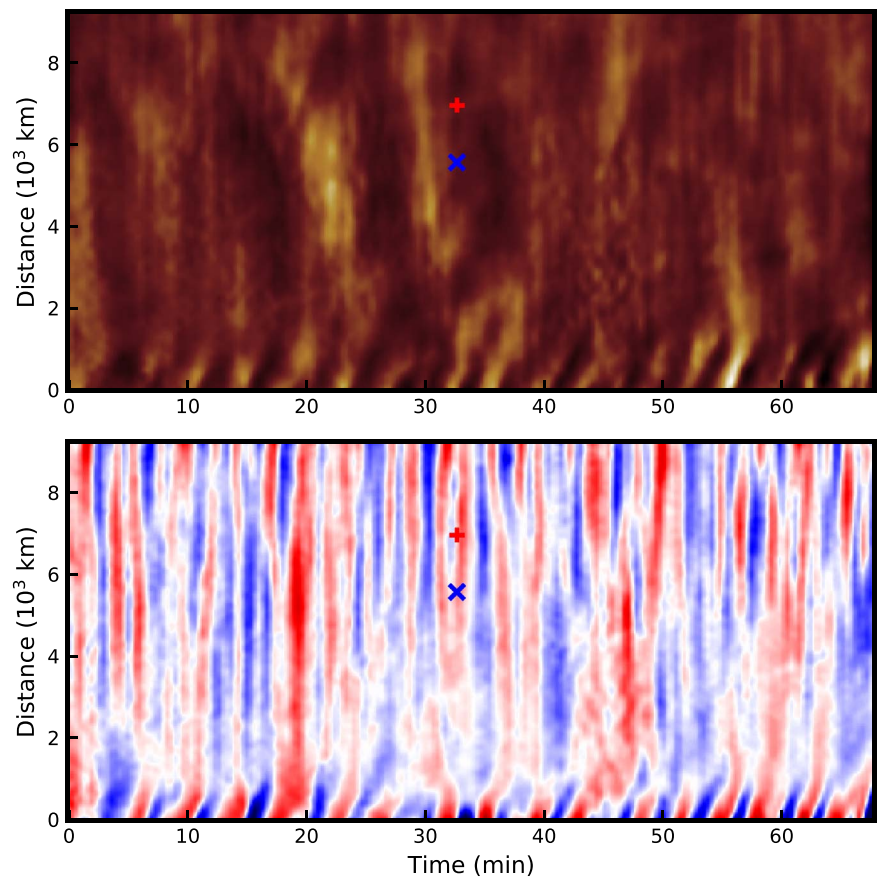


Figure 5. Time–distance plot of intensity and velocity constructed along the thick green curve shown in Figure 3. Both intensity and velocity are band filtered (1.0–21 minutes). The distance is measured from the footpoint. The cross and plus sign mark the position and central time of velocity oscillations at points *X* and *Y* selected for illustration, respectively.

respectively, indicating that c of 3-minute waves is 141 km s⁻¹ on average and ranges from 32 to 620 km s⁻¹. In contrast, the propagation speed of the 10-minute waves is 63 km s⁻¹ on average and ranges from 12 to 330 km s⁻¹. The above speed range of the 3-minute waves includes all the speeds from 40 to 150 km s⁻¹ reported by Chae et al. (2021b). The speed range of the 10-minute waves practically includes all the speeds from 10 to 70 km s⁻¹ reported by Morton et al. (2021).

The direction of propagation—either outward from the sunspot center or inward to it—is another interesting property of the identified wave packets. Interestingly, we found that the statistics on the propagation direction strongly depends on the group (see the top of the figure). In the group of 3-minute waves, most (77%) of the waves propagated outward from the sunspot center, with the remaining 23% propagating inward toward the sunspot center. In contrast, in the other group of 10-minute waves, about half (49%) of the waves propagated outward and the other half (51%) propagated inward, indicating the statistical balance between the outward and inward propagation.

Next, we examine the statistics of velocity amplitude V. In the 3-minute waves, the mean and the standard deviation of $\log V$ are estimated at -0.18 and 0.16, indicating that V of the 3-minute waves is 0.66 km s^{-1} on average and ranges from 0.32 to 1.4 km s^{-1} . In the same manner, it is found that V of the 10-minute waves is 0.63 km s^{-1} on average and ranges from 0.25 to 1.6 km s^{-1} . Thus, we do not find any significant difference in the statistics of V between the two groups of waves. The above ranges of V include 1.0 km s^{-1} , which is the

reported amplitude of both horizontal velocity oscillation (Pietarila et al. 2011) and line-of-sight velocity oscillation (Chae et al. 2021b). They also coincide well with the reported range of horizontal velocity oscillation from 0.4 to 1.0 km s⁻¹ (Morton et al. 2021).

3.5. Correlations between Parameters

It can be seen from the top of Figure 8 that propagation speed c is negatively correlated with period P. The correlation is not strong because of the large fluctuation of c for a given P. The Pearson correlation coefficient between $\log c$ and $\log P$ is estimated at -0.48. At any rate, this indicates that the waves of shorter periods tend to have higher speeds than the waves of longer periods, confirming the result above that the 3-minute waves have statistically higher propagation speeds than the 10-minute waves.

The middle panel of Figure 8 shows the dependence of velocity amplitude on period. It can be seen from the figure that $\log V$ is the largest around $\log P = 0.5$ (3.2 minutes), tends to decrease with period, and becomes the smallest around $\log P = 0.85$ (7.1 minutes). At longer periods, $\log V$ tends to increase with period, reaches a peak around $\log P = 1.1$ (12.6 minutes), and decreases with period. This behavior is very similar to that of the histogram of $\log P$ shown in the top of Figure 7. This behavior is another evidence that there exist two distinct groups of waves: 3-minute period waves and 10-minute period waves.

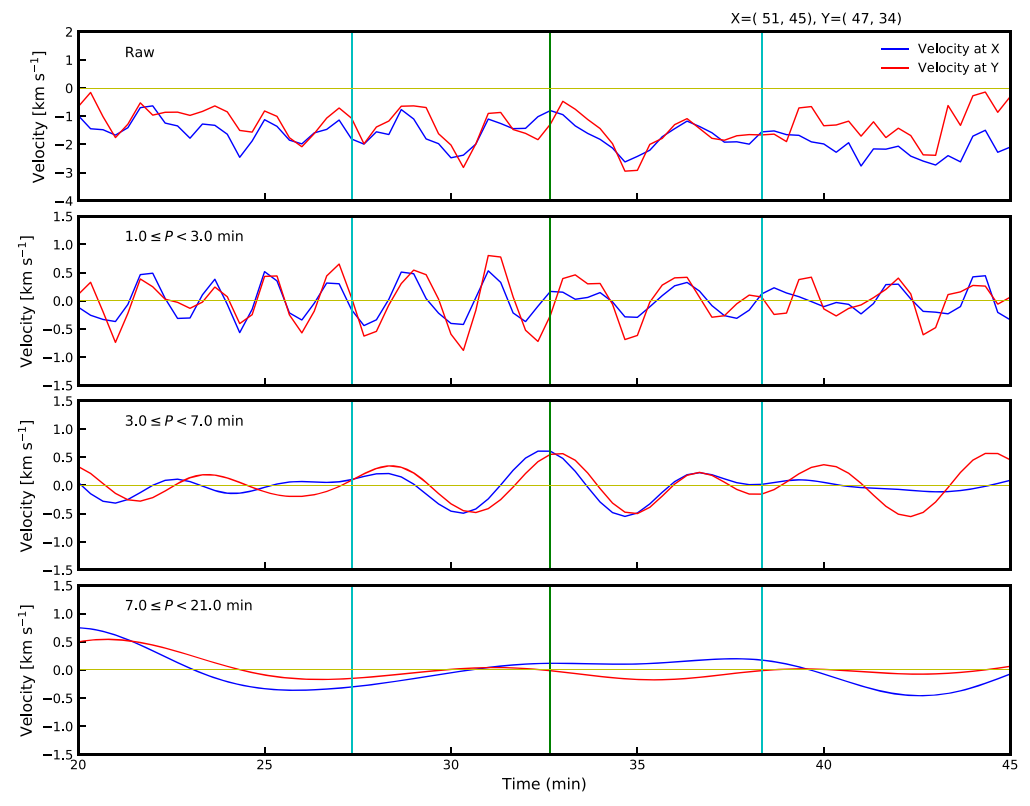


Figure 6. Time variations of $H\alpha$ original LOS velocity, and band-filtered velocities at two points. The data from point X (marked by a cross in Figure 3) are plotted in blue and those from Y (marked by a plus sign) in red. Each step corresponds to the time interval of 20 s. Two cyan vertical lines in each plot indicate start time t_1 and end time t_2 manually chosen for the correlation analysis. The green vertical line indicates the observing time of the maps presented in Figure 3.

It is also interesting to examine the dependence of propagation speed c on the distance d from the sunspot center. The bottom of the figure indicates that there is a weak positive correlation between $\log c$ and d with the correlation coefficient of 0.38, meaning that waves at farther distances tend to have faster propagation speeds. Figure 8 also indicates that 3-minutes waves tend to be detected at farther distances than 10-minute waves. It is noteworthy that despite these statistical tendencies, $\log c$ has large statistical fluctuations even with the same values of P and d. This suggests that there is a physical factor that is more fundamental than period and distance in determining propagation speed. In Section 4, we will argue that mass density has to be considered as the most important factor determining propagation speed.

3.6. Spatial Distribution

Figure 9 presents the spatial distribution of wave packets detected during a time interval. Note that the wave packets are best detected in well-defined velocity stripes. This may be because the spatiotemporal pattern of velocity in these features is simple enough for an easy identification of wave packets there. Wave packets may also occur in the features displaying complex spatiotemporal patterns of velocity, but their identification is not easy because of the complexity of velocity patterns. Thus, we admit that our detection of Alfvénic waves may not be complete in the spatial sampling and there might be a bias in the spatial distribution of detected waves. Despite this, the spatial distribution can provide us with some physical information.

The figure clearly shows that a small area often hosts wave packets of different propagation speeds and different periods. Two oppositely directed wave packets often occur side by side within a small area, not only when they have different periods but also when they have similar periods. We also find that 3-minute waves and 10-minute waves are not spatially exclusive to each other. They can occur even on the same position on the image plane, as clearly illustrated in Figure 10, presenting the wavelet power spectrum constructed from the time series of velocity at a point. This wavelet power spectrum displays not only the oscillations of periods of 3–5 minutes but also those of periods of 9–20 minutes. This wavelet spectrum is similar to one of the wavelet spectra reported by Chae et al. (2021b).

This coexistence of wave packets of different periods, however, does not necessarily mean the physical coexistence of different wave packets on the same volume. If they really occur on the same volume so that their coexistence could be regarded as the linear superposition of waves of different periods, they should have the same propagation speed. But we find that the wave packets of different periods usually have different propagation speeds.

The mixture and the apparent coexistence of different wave packets may be best understood if a sizable chromospheric volume comprises numerous thin magnetic flux tubes carrying individual Alfvénic waves of different periods at different speeds. If their diameters are smaller than the spatial resolution in the horizontal direction and the vertical extent over which the ${\rm H}\alpha$ line core is formed, the observations will often display the mixture of different waves in a small area on the image

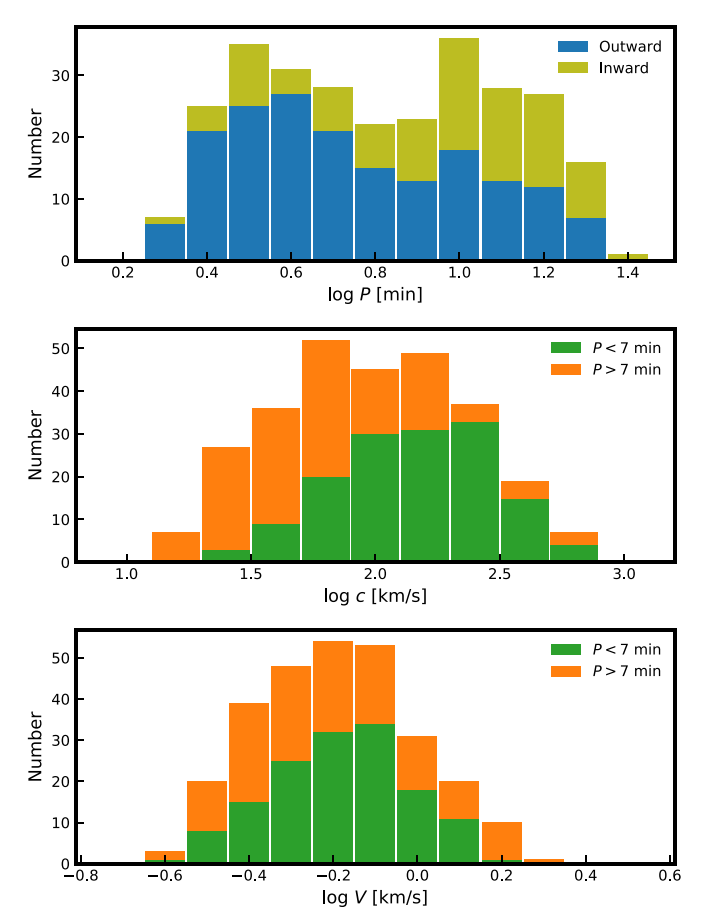


Figure 7. Stacked histograms of period $(\log P)$, propagation speed $(\log C)$, and velocity amplitude $(\log V)$, distinguishing either between outward waves and inward waves or between short-period waves and long-period waves.

plane, and even the apparent coexistence of different waves at the same position on the image plane.

4. Discussion

4.1. Alfvénic Waves in the Chromosphere

We have identified each wave packet by examining the cross-correlation of LOS velocity oscillations at two points manually selected along the same velocity stripe. The identified wave packets are quite compatible with Alfvénic waves or transverse magnetohydrodynamic waves propagating along magnetic fields. The velocity stripes are usually cospatial or parallel with intensity threads and fibrils that are likely to trace magnetic field lines that are highly inclined to the horizontal. Thus, the observed LOS velocity oscillations mostly reflect the oscillations of velocity transverse to magnetic field lines. These velocity oscillations are not correlated with any noticeable intensity oscillations, suggesting that the waves are incompressive or very weakly compressive. Moreover, we found that these oscillations are found to propagate along the fibrils and threads at speeds that are supersonic and compatible with Alfvén speeds in the solar chromosphere. In this regard, our study confirms the spectroscopic detection of Alfvénic waves in the sunspot chromosphere first done by Chae et al. (2021b).

Our study in fact reveals many new aspects of the Alfvénic waves in the chromosphere thanks to the systematic measurement of the parameters of a large number of wave packets.

First, we note that the measured propagation speeds range from 12 to 620 km s⁻¹. We attribute this large variation to the inhomogeneity of mass density in the fibrils. The theoretical speed of Alfvénic waves (kink waves) propagating along a magnetic flux tube in the upper chromosphere is given by

$$c = \frac{B}{\sqrt{4\pi\rho}} \tag{8}$$

with magnetic field $B \approx B_i \approx B_e$ and average mass density $\rho \equiv (\rho_i + \rho_e)/2$, where the subscripts i and e refer to the values in the internal and external regions of the flux tube, respectively. By identifying the observed propagation speeds with this theoretical speed and by adopting B=150 G for magnetic field strength at the distance of 5000 km, for instance, we can attribute the range of propagation speed from about 30 to about 300 km s⁻¹ observed at the same distance mostly to the variation of ρ from 2×10^{-10} g cm⁻³ to 2×10^{-12} g cm⁻³. This range of mass density is found in the chromosphere, for instance, at heights from 950 to 1740 km according to the standard atmospheric model for a plage region (Model P; Fontenla et al. 1993).

As the real atmosphere is horizontally inhomogeneous, unlike the standard model, mass density can vary even in the horizontal direction. In this regard, the dependence of ρ and c on z is meaningful only in a statistical sense. The layers of higher z will have statistically lower values of ρ and higher values of c than the layers of lower c. Our observations strongly suggest that the real chromosphere of the superpenumbral region around the sunspot comprises numerous thin magnetic flux tubes along which Alfvénic waves propagate. It is very likely that density and propagation speed vary much from flux tube to flux tube. The observable consequence is the mixture and the apparent coexistence of waves of different speeds and different directions of propagation.

Very important is our identification of two groups of Alfvénic waves: 3-minute period waves and 10-minute period waves. The 3-minute waves we detected must be the same kind of waves detected by Chae et al. (2021b). The 10-minute waves we detected using the spectroscopic method seem to be of the same kind as the Alfvénic waves detected by Morton et al. (2021) using the imaging method, in that the two period ranges are much overlapping each other. The major difference between these two groups is in the direction of velocity oscillation. The waves we detected oscillate noticeably in the LOS direction or in the vertical direction, and the waves detected by Morton et al. (2021) oscillate noticeably in the transverse direction or in the horizontal direction. Note that 10minute period oscillations were previously detected in dynamic fibrils of sunspot regions (Maurya et al. 2013; Chae et al. 2014), but these oscillations are not Alfvénic waves but slow magnetoacoustic waves. On the contrary, the 10-minute oscillations seen in a wavelet power spectrum of LOS velocity presented by Chae et al. (2021b) seem to represent Alfvénic waves detected by the spectroscopic method.

The physical significance of the Alfvénic waves we identified may be quantified in terms of wave energy density

$$U = \frac{1}{2}\rho V^2 = \frac{B^2}{8\pi} \left(\frac{V}{c}\right)^2 \tag{9}$$

Table 1
Mean Values and Standard Deviations of Physical Parameters for the 3-minute Waves, the 10-minute Waves, and All the Waves

Parameter	3-minute Waves	10-minute Waves	All Waves
log P, period (minutes)	0.57 ± 0.14	1.08 ± 0.13	0.81 ± 0.29
$\log c$, propagation speed (km s ⁻¹)	2.15 ± 0.32	1.80 ± 0.36	2.00 ± 0.41
$\log V$, velocity amplitude (km s ⁻¹)	-0.18 ± 0.16	-0.20 ± 0.20	-0.22 ± 0.20
Outward propagation fraction (%)	77	49	64
$\log U$, energy density (erg cm ⁻³)	-1.91 ± 0.85	-0.88 ± 1.11	-1.41 ± 1.11
$\log F$, energy flux (erg cm ⁻² s ⁻¹)	5.24 ± 0.60	5.92 ± 0.86	5.57 ± 0.81

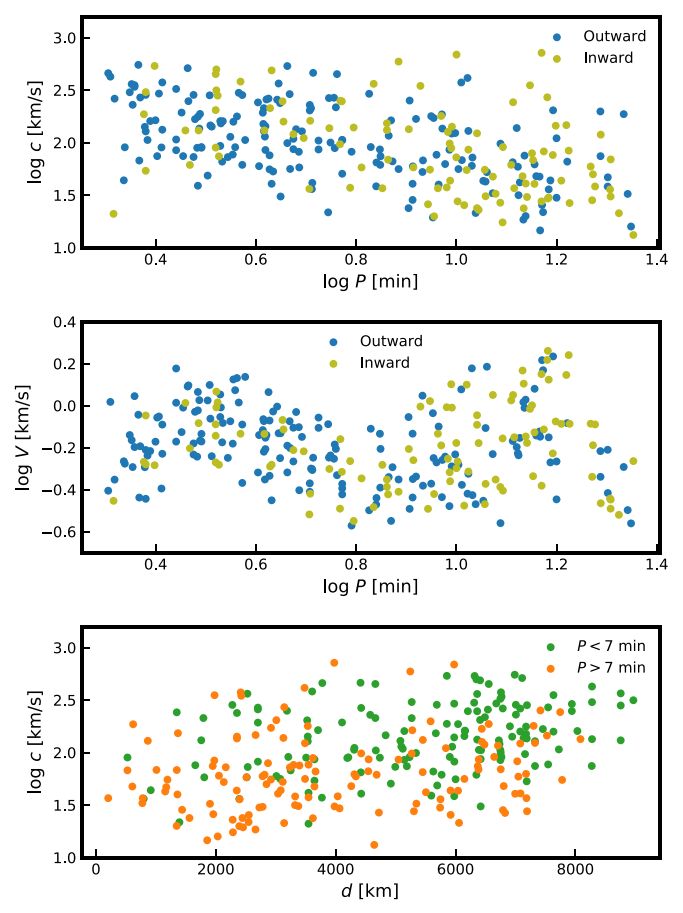


Figure 8. Scatter plots showing $\log c$ vs. $\log P$ (top), $\log V$ vs. $\log P$ (middle), and $\log c$ vs. $\log d$ (bottom).

and wave energy flux

$$F = \frac{1}{2}\rho V^2 c = \frac{B^2}{8\pi} \left(\frac{V}{c}\right)^2 c,$$
 (10)

with the assumption of the equipartition between kinetic energy and magnetic energy in the waves. Note that V here denotes velocity amplitude and the kinetic energy density of waves is equal to $\rho V^2/4$.

Figure 11 presents the number distributions of $\log U$ and $\log F$ calculated by using the values of B inferred from the extrapolation as shown in Figure 2. The mean values and the ranges of $\log U$ (cgs unit) and $\log F$ are listed in Table 1 for 3-minute waves and 10-minute waves, respectively. These numeric values indicate that the mean energy density and flux of the 10-minute waves are significantly larger than those of the 3-minute waves. The reason for this is obvious from

Equations (9) and (10). As there is little difference in V between the two groups, the difference in U and F should be attributed to the difference in c and d. The 10-minute waves tend to be detected with lower values of d and at closer distances that have higher values of d. Therefore, the 10-minute waves occur at high mass density regions and have higher energy density and flux.

Interestingly, averaging $\log U$ over all the waves yields $3.9 \times 10^{-2} \, \mathrm{erg \, cm^{-3}}$, which happens to be close to $4.0 \times 10^{-2} \, \mathrm{erg \, cm^{-3}}$ chosen by Laming (2004) to explain the observed fractionization of the low first ionization potential (FIP) elements. The mean value of $\log F$ over all the waves corresponds to $3.7 \times 10^5 \, \mathrm{erg \, cm^{-2} \, s^{-1}}$, which is in the range of $2.6 \times 10^5 \, \mathrm{erg \, cm^{-2} \, s^{-1}}$ to $1.0 \times 10^6 \, \mathrm{erg \, cm^{-2} \, s^{-1}}$ estimated for the Alfvénic waves detected by Chae et al. (2021b).

4.2. A Tale on the 3-minute Alfvénic Waves

Our new finding is the presence of two groups of Alfvénic waves: 3-minute waves and 10-minute waves. This finding leads us to think of two tales on the origin of Alfvénic waves. First, we conjecture that the 3-minute waves are excited by the upward-propagating slow magnetoacoustic waves in the sunspot. It is, however, not clear yet how this slow-to-Alfvénic mode conversion occurs in the solar atmosphere. Chae et al. (2021b) proposed a simple mechanism that slow waves propagating upward along the vertical field lines excite transverse waves propagating along the horizontal field lines when magnetic field lines are highly bent from the vertical to the horizontal, as schematically illustrated in Figure 12. This idea is supported by the observed time-distance plots of velocity and intensity in Figure 5, indicating that some slow waves near the footpoint are spatially and temporarily connected to the Alfvénic waves in the fibril regions.

This mechanism, however, has a couple of theoretical problems that need to be resolved. One is that as plasma β in the chromosphere may be much lower than 1, slow waves may propagate, being rigidly confined to the field lines and not being able to perturb magnetic field in the transverse direction even if field lines are bent. As for this problem, we note that the slow waves nonlinearly develop into shocks as they propagate upward, significantly enhancing local pressure and local plasma β , so that slow waves may be able to disturb magnetic fields. This possibility is indirectly supported by the observations of penumbral running waves that resulted in the 200 G change of field strength (de la Cruz Rodríguez et al. 2013) and umbral flashes that caused transversal magnetic field fluctuation up to 200 G (Houston et al. 2018). These observations suggest that the less strong modification of magnetic field by slow waves may occur in the solar chromosphere more frequently.

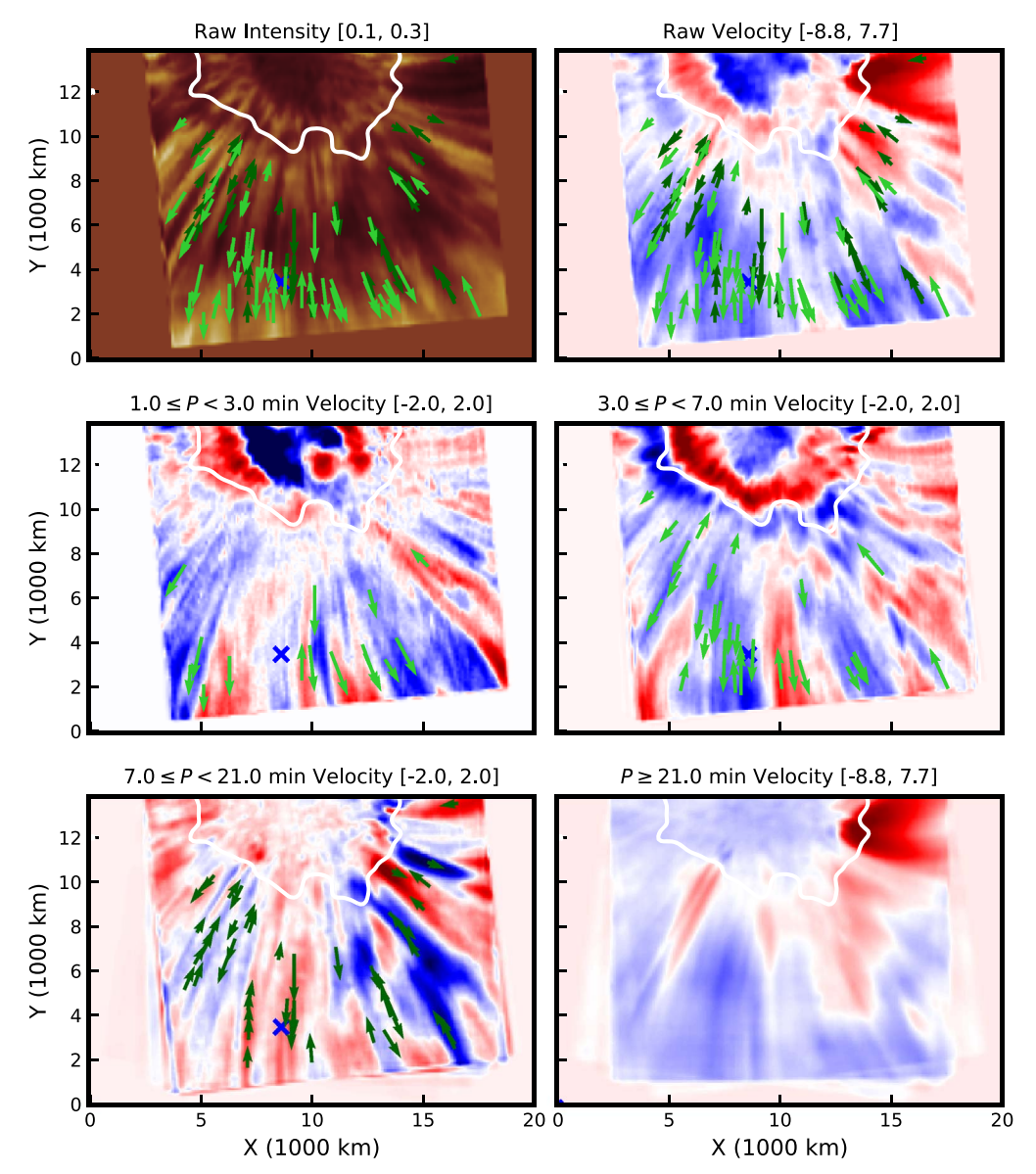


Figure 9. Spatial distribution of 94 wave packets, the peaks of which occurred during the same time interval of 15 minutes. The underlying maps are the maps constructed at the middle of the time interval. Each arrow represents a wave packet. Its center indicates the middle position of two points selected for cross-correlation analysis; its direction, the direction of wave propagation; and its length, the nonlinear scaling of propagation speed ($\propto c^{1/3}$), with the shortest and longest ones corresponding to 16 and 590 km s⁻¹, respectively. The light-green arrows represent 3-minute waves of period <7 minutes; dark-green arrows, 10-minute waves of period >7 minutes. In the maps of intensity and raw velocity, all of the 94 wave packets are indicated, but in each map of passband-filtered velocity, only the wave packets with period belonging to the passband are indicated. Marked by the cross is the point where the velocity variation shown in Figure 10 was extracted.

The other problem is that, in general, slow-to-Alfvénic mode conversion can occur only at regions where slow speed and Alfvén speed are comparable. For these reasons, slow-to-Alfvén mode conversion was considered to take place in the lower solar atmosphere (Raboonik & Cally 2019; Cally 2022) or in the $\beta=1$ interface of a sunspot region (Grant et al. 2018). As for this problem, we note that the conversion may occur at a lower level than the layers where Alfvénic waves are detected. At this level, mass density may be much higher and the Alfvén speed may be much lower than the lowest value of the propagation speed we obtained, which is 12 km s $^{-1}$. This value is very comparable to 10 km s $^{-1}$, a typical sound speed in the chromosphere.

At any rate, if Alfvénic waves are excited by the slow-to-Alfvénic mode conversion, their period should be the same as the exciting slow waves. Therefore, the origin of the period in the slow waves has to be explained. The period of slow waves like 3-minute umbral oscillations is closely related to the acoustic cutoff of the atmosphere. In an isothermal atmosphere, the acoustic cutoff frequency is given by the Lamb frequency

$$\omega_{\rm ac} = \frac{c_a}{2H},\tag{11}$$

with acoustic wave speed c_a and pressure scale height H. In a nonisothermal atmosphere, however, the acoustic cutoff frequency is not even uniquely defined, not to speak of differing from the Lamb frequency (see, e.g., Chae & Litvinenko 2018). More important is the finding that even if it can be defined somehow, the acoustic cutoff frequency does not sharply separate between propagating waves and non-propagating waves. Therefore, Chae & Litvinenko (2018)

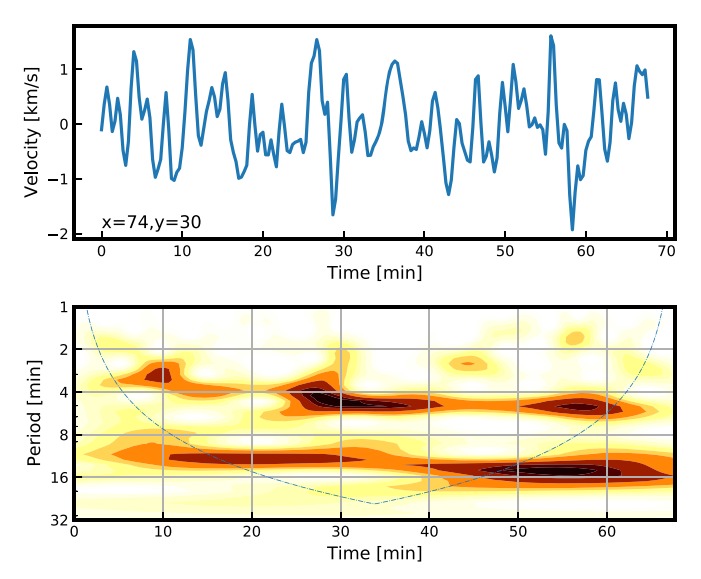


Figure 10. Plots of velocity variation at the point marked by the cross in Figure 9 (top) and its wavelet power spectrum (bottom).

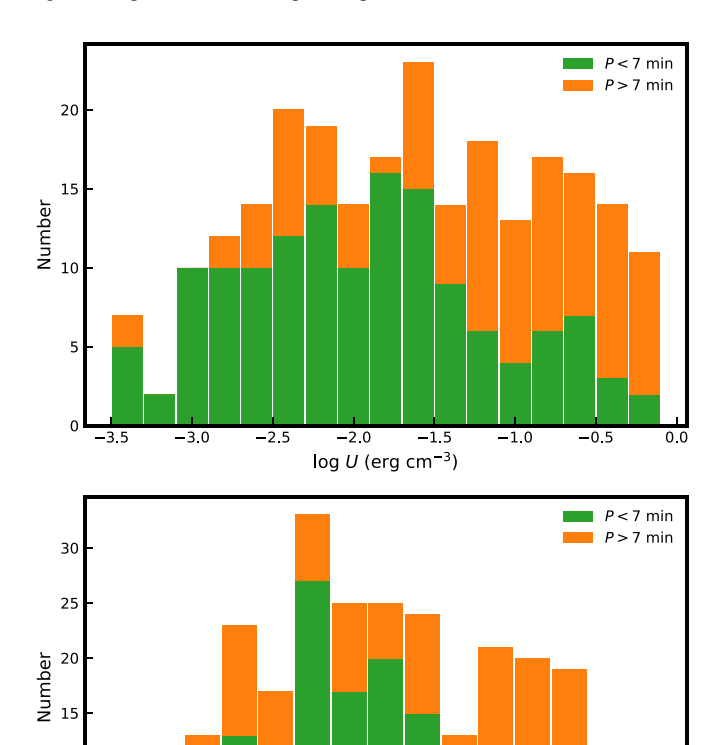


Figure 11. Stacked histograms of wave energy density (log U) and wave energy flux (log F) calculated by assuming $B=100~\rm G$ distinguishing between 3-minute (P<7 minutes) waves and 10-minute (P>7 minutes) waves.

 $\log F \text{ (erg cm}^{-2} \text{ s}^{-1}\text{)}$

10

suggested that the acoustic cutoff frequency should be understood as the center of the frequency band where the transition from low acoustic transmission to high transmission takes place. In other words, the acoustic cutoff frequency in a nonisothermal atmosphere is the frequency at which half of the waves propagates, and the other half does not propagate. This

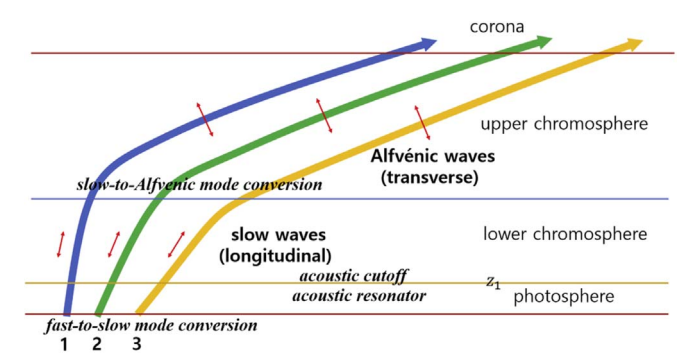


Figure 12. Illustration of the tale for 3-minute Alfvénic waves. The three curved arrows indicate magnetic field lines (or magnetic flux tubes) with different inclinations in the photosphere.

property added a new feature of the acoustic cutoff in the solar atmosphere: to establish a photospheric acoustic resonator (Chae et al. 2019). The acoustic cutoff frequency of the whole atmosphere is represented by the biggest value of $\omega_{\rm ac}$, which occurs at temperature minimum. The volume between the photospheric or subphotospheric driver and the temperature minimum acts like an emitting resonator: accumulating and emitting wave energy at the acoustic resonance frequency ω_a , which is about 1.05 times the local peak of $\omega_{\rm ac}$ at z_1 near the photosphere or

$$\omega_a = 1.05\omega_{\rm ac}(z_1),\tag{12}$$

where z_1 is practically the height of temperature minimum (see Figure 12). Thus, not only the resonant period of the slow waves but also the period of the Alfvénic waves excited by these waves is given by

$$P_a = \frac{4\pi}{1.05} \frac{c_1}{\gamma g \cos \theta} = 3.0 \text{ minutes} \frac{1}{\cos \theta} \left(\frac{T_1}{4300 \text{ K}}\right)^{1/2}, \quad (13)$$

with the choice of specific heat ratio $\gamma=1.67$, mean molecular weight $\mu=1.25$, and solar surface gravity $g=27,400~{\rm cm~s^{-2}}.$ This formula indicates that the period is determined by temperature T_1 and θ at z_1 , the level of temperature minimum through which the wave-guiding field lines pass. At the center of a sunspot, T_1 is low, and θ is almost zero, so that period P is the shortest. With distance from the sunspot center, both T_1 and θ increase, so P also increases.

The temperature T_1 can be as low as 3300 K in sunspot umbrae (Maltby et al. 1986) and as high as 4900 K in plages (Fontenla et al. 1993), so P is expected to range from 2.6 to 3.2 minutes when magnetic field lines are vertical. As the inclination θ usually increases with distance from the sunspot center, P is also expected to increase with distance. For example, θ increases from zero to, say, 60° , and P increases by a factor of 2. Thus, the combined effect of T_1 and θ is able to explain for the period from 2.6 to 6.4 minutes, which is quite compatible with the period range of the detected 3-minute Alfvénic waves.

4.3. A Tale on the 10-minute Alfvénic Waves

The 10-minute Alfvénic waves are not likely to be excited by the mode conversion of slow waves, and we have to think of other possibilities. We propose that the observed 10-minute Alfvénic waves represent the chromospheric manifestation of

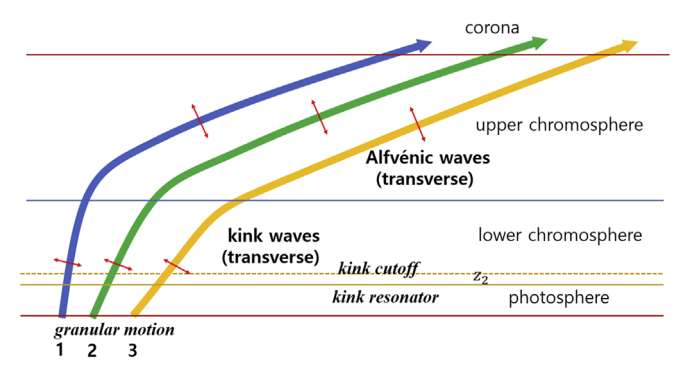


Figure 13. Illustration of the tale for 10-minute Alfvénic waves.

the kink waves that are exited by convective motions in the photosphere. Convective motions are quite common outside strong field regions. They can occur even inside strong field regions in the form of magnetoconvection. As illustrated in Figure 13, when the photospheric parts of magnetic field lines (or flux tubes) are subject to agitating convective motions, kink waves may be excited by these motions. We suppose that these kink waves can propagate upward to the chromosphere along field lines that are predominantly vertical in the photosphere. If this is the case, the direction of velocity oscillation should change from the predominantly horizontal direction to the predominantly vertical direction, which needs some physical explanation that we do not have yet. In contrast, in the Alfvénic waves that were detected by the imaging method (Morton et al. 2021), the change of velocity oscillation direction is not required because these waves display velocity oscillations in the horizontal direction. In either case, we assume that the 10minute Alfvénic waves detected in the chromosphere originate from the kink waves excited by the convective motions in the photosphere.

We conjecture that the periods of 10-minute waves may be related to the cutoff of the kink waves near the temperature minimum. Spruit (1981) first indicated that the kink waves in the atmosphere are subject to cutoff like acoustic waves. He estimated the cutoff period at 11.7 minutes. According to the calculation by Cranmer & van Ballegooijen (2005), the cutoff period has a minimum of 9.7 minutes at a height of 200 km. Interestingly, these periods are comparable to those of the longperiod Alfvénic waves we measured in the present work. However, it was realized later by Lopin & Nagorny (2013) that kink waves in an *isothermal* atmosphere are in fact cutoff-free, and the finding of the cutoff by Spruit (1981) erroneously resulted from the neglect of the radial component of an unperturbed tube magnetic field. Nevertheless, in a nonisothermal atmosphere, kink waves can have cutoff. According to Lopin & Nagorny (2017), the local kink cutoff frequency like $\omega_{\rm ac}$ is given by

$$\omega_{\rm kc} = \frac{c_k}{2H} \left(\frac{dH}{dz}\right)^{1/2} = \omega_{\rm ac} \left(\frac{2}{\gamma(2\beta+1)} \frac{dH}{dz}\right)^{1/2},\tag{14}$$

with kink wave speed c_k and plasma beta β inside the flux tube. Note that $\omega_{\rm kc}$ is zero at regions $dH/dz \le 0$ and has a local peak at a height z_2 a little above the temperature minimum (see the bottom panel of Figure 12). This local peak of $\omega_{\rm kc}$ may act like the peak of $\omega_{\rm ac}$ occurring at the temperature minimum. That is, as the atmosphere is nonisothermal, the kink cutoff frequency $\omega_{\rm kc}(z_2)$ should be understood as the frequency at which half the

waves transmit upward and the other half get reflected back downward. Therefore, we can expect that the volume between z_2 and the level of the photospheric or subphotospheric driver becomes a resonating emitter of kink waves like the acoustic resonator proposed by Chae et al. (2019). The kink resonator is then expected to have a resonance frequency that is above, but very close to, the peak of $\omega_{\rm kc}(z_2)$. If we adopt the same value 1.05 as the ratio of the resonance frequency to the peak of $\omega_{\rm kc}(z_2)$,

$$\omega_k = 1.05 \omega_{\rm kc}(z_2),\tag{15}$$

the resonance kink period is given by

$$P_k = 9.0 \text{ minutes} \frac{1}{\cos \theta} \left(\frac{T_2}{4650 \text{ K}} (2\beta + 1) \frac{0.1}{(dH/dz)_2} \right)^{1/2},$$
(16)

where the subscript 2 is used to denote the values at z_2 . With the atmospheric model C for the average quiet regions (FALC model) of Fontenla et al. (1993), we obtain $z_2 = 680$ km, $(dH/dz)_2 = 0.124$, and $T_2 = 5050$ K. Therefore, with $\beta = 0.5$ and $\theta = 0$, we obtain $P_k = 11.9$ minutes. With a smaller value $\beta = 0.1$ (corresponding to stronger field), we have a new estimate of 9.2 minutes. These estimates are consistent with the peak of 10 minutes in the observed distribution of periods. Moreover, if we take into account the effect of inclination variation from $\theta = 0^\circ$ to 60° , as well as the above variation of β from 0.10 to 0.5, the period of the kink waves is expected to vary from 9 to 22 minutes. This range of period is very consistent with the observed periods of the long-period Alfvénic waves.

5. Conclusion

Our results are solid evidence that Alfvénic waves of significant energy prevail in the chromosphere of active regions. They also strongly suggest that the chromosphere of the region around the sunspot comprises numerous thin magnetic flux tubes with different mass density along which Alfvénic waves excited by the same source may propagate at different speeds. An important new finding of our study is that the Alfvénic waves are clearly separated into two groups, 3-minute period waves and 10-minute period waves, which strongly suggests that there are two tales on the origin of the Alfvénic waves. Based on our results, we have proposed that the 3-minute Alfvénic waves are excited by the slow-to-Alfvénic mode conversion in the chromosphere and the 10minute Alfvénic waves are excited by granular motions agitating thin magnetic flux tubes in the photosphere or a subphotospheric layer.

Further observational works and theoretical works are definitely needed to clarify the physical nature and origins of Alfvénic waves we detected in the chromosphere of sunspot regions. It also would be interesting to extend the investigation of Alfvénic waves to other solar regions under diverse magnetic environments.

We are grateful to the referee for constructive comments and suggestions. This research was supported by the National Research Foundation of Korea (NRF-2020R1A2C2004616 and NRF-2020R1I1A1A01068789). E.-K.L. was supported by the

Korea Astronomy and Space Science Institute under the R&D program supervised by the Ministry of Science and ICT. J.K. was supported by the Korea Astronomy and Space Science Institute under the R&D program (project No. 2022-1-850-07). The GST operation is partly supported by the Korea Astronomy and Space Science Institute, the Seoul National University, and the Key Laboratory of Solar Activities of Chinese Academy of Sciences (CAS) and the Operation, Maintenance and Upgrading Fund of CAS for Astronomical Telescopes and Facility Instruments.

ORCID iDs

Jongchul Chae https://orcid.org/0000-0002-7073-868X Kyuhyoun Cho https://orcid.org/0000-0001-7460-725X Eun-Kyung Lim https://orcid.org/0000-0002-7358-9827 Juhyung Kang https://orcid.org/0000-0003-3540-4112

References

```
Beckers, J. M., & Tallant, P. E. 1969, SoPh, 7, 351
Bloomfield, D. S., Lagg, A., & Solanki, S. K. 2007, ApJ, 671, 1005
Cally, P. S. 2022, MNRAS, 510, 1093
Cally, P. S., & Hansen, S. C. 2011, ApJ, 738, 119
Chae, J., Cho, K., Kang, J., et al. 2021a, JKAS, 54, 139
Chae, J., Cho, K., Nakariakov, V. M., Cho, K.-S., & Kwon, R.-Y. 2021b, ApJL, 914, L16
Chae, J., Kang, J., & Litvinenko, Y. E. 2019, ApJ, 883, 72
Chae, J., & Litvinenko, Y. E. 2017, ApJ, 844, 129
Chae, J., & Litvinenko, Y. E. 2018, ApJ, 869, 36
Chae, J., Madjarska, M. S., Kwak, H., & Cho, K. 2020, A&A, 640, A45
Chae, J., Park, H.-M., Ahn, K., et al. 2013, SoPh, 288, 1
Chae, J., Song, D., Seo, M., et al. 2015, ApJL, 805, L21
```

```
Chae, J., Yang, H., Park, H., et al. 2014, ApJ, 789, 108
Cho, K., & Chae, J. 2020, ApJL, 892, L31
Cho, K., Chae, J., Lim, E.-k., & Yang, H. 2019, ApJ, 879, 67
Cranmer, S. R., & van Ballegooijen, A. A. 2005, ApJS, 156, 265
de la Cruz Rodríguez, J., Rouppe van der Voort, L., Socas-Navarro, H., &
   van Noort, M. 2013, A&A, 556, A115
de la Cruz Rodríguez, J., & Socas-Navarro, H. 2011, A&A, 527, L8
De Pontieu, B., McIntosh, S. W., Carlsson, M., et al. 2007, Sci, 318, 1574
Fontenla, J. M., Avrett, E. H., & Loeser, R. 1993, ApJ, 406, 319
Giovanelli, R. G. 1972, SoPh, 27, 71
Goode, P. R., Coulter, R., Gorceix, N., Yurchyshyn, V., & Cao, W. 2010, AN,
  331, 620
Grant, S. D. T., Jess, D. B., Zaqarashvili, T. V., et al. 2018, NatPh, 14, 480
He, J. S., Tu, C. Y., Marsch, E., et al. 2009, A&A, 497, 525
Houston, S. J., Jess, D. B., Asensio Ramos, A., et al. 2018, ApJ, 860, 28
Jess, D. B., Pascoe, D. J., Christian, D. J., et al. 2012, ApJL, 744, L5
Kang, J., Chae, J., Nakariakov, V. M., et al. 2019, ApJL, 877, L9
Khomenko, E., & Cally, P. S. 2012, ApJ, 746, 68
Laming, J. M. 2004, ApJ, 614, 1063
Leenaarts, J., Carlsson, M., & Rouppe van der Voort, L. 2015, ApJ, 802,
Lopin, I., & Nagorny, I. 2013, ApJ, 774, 121
Lopin, I., & Nagorny, I. 2017, ApJ, 840, 26
Maltby, P., Avrett, E. H., Carlsson, M., et al. 1986, ApJ, 306, 284
Maurya, R. A., Chae, J., Park, H., et al. 2013, SoPh, 288, 73
Morton, R. J., Mooroogen, K., & Henriques, V. M. J. 2021, RSPTA, 379,
Pietarila, A., Aznar Cuadrado, R., Hirzberger, J., & Solanki, S. K. 2011, ApJ,
   739, 92
Raboonik, A., & Cally, P. S. 2019, SoPh, 294, 147
Spruit, H. C. 1981, A&A, 98, 155
Tomczyk, S., McIntosh, S. W., Keil, S. L., et al. 2007, Sci, 317, 1192
Torrence, C., & Compo, G. P. 1998, BAMS, 79, 61
Van Doorsselaere, T., Nakariakov, V. M., & Verwichte, E. 2008, ApJL,
  676, L73
Zhao, J., Chen, R., Hartlep, T., & Kosovichev, A. G. 2015, ApJL, 809, L15
Zirin, H., & Stein, A. 1972, ApJL, 178, L85
```